Physics of Fluids

RESEARCH ARTICLE | JULY 10 2023

# Numerical study of the geometric characteristics and kinetic behavior of single bubble rise processes in different liquids

Li Yixin (李一鑫) ; Yang Na (杨娜); Xiao Xiaoming (肖晓明); Jiang Bin (姜斌); Sun Yongli (孙永利); Zhang Luhong (张吕鸿)



*Physics of Fluids* 35, 073310 (2023)
https://doi.org/10.1063/5.0150547

Physics of Fluids ARTICLE pubs.aip.org/aip/pof

# Numerical study of the geometric characteristics and kinetic behavior of single bubble rise processes in different liquids

Cite as: Phys. Fluids **35**, 073310 (2023); doi: 10.1063/5.0150547
Submitted: 15 March 2023 · Accepted: 19 June 2023 ·
Published Online: 10 July 2023



Yixin Li (李一鑫), Na Yang (杨娜), Xiaoming Xiao (肖晓明), Bin Jiang (姜斌), Yongli Sun (孙永利), and Luhong Zhang (张吕鸿)[a]

## AFFILIATIONS

School of Chemical Engineering and Technology, Tianjin University, Tianjin 300072, People's Republic of China

[a]Author to whom correspondence should be addressed: zhanglvh@tju.edu.cn. Tel./Fax: +86 22 27400199

## ABSTRACT

The characterization of single bubble in gas–liquid two phase flow is a critical yet unresolved issue in both science and industry. In this study, the volume-of-fluid (VOF) method is used to numerically simulate and experimentally investigate the effect of initial bubble diameter, liquid viscosity, and surface tension on bubble deformation and the internal flow field of the bubble in a pool of stationary liquid. The findings indicate that as liquid viscosity increases, the bubble's rising speed decreases, and the bubble tends to oscillate. The variation in bubble deformation ratio and the degree of fluctuation increase with the bubble's initial diameter and decrease with the viscosity of the liquid phase. Additionally, as the surface tension of the liquid decreases, the bubble becomes more prone to rupture, and the number of ruptures increases. The flow field inside the bubble can be classified into three categories: "double main vortex type," "double main vortex type with separated vortex," and "double main vortex type with scattered vortex." The velocity reaches its maximum at the center of each vortex type, and the velocity at the interface varies as the bubble interface shape changes. This work lays the foundation for the study of the flow field inside the bubble and improves the predictability of gas–liquid equipment design.





## I. INTRODUCTION

The considerable growth in global population and rapid industrial expansion is undeniable indicators of human societal progress. However, they may also lead to adverse economic and social consequences, such as natural resource scarcity and ecosystem degradation.[1,2] As a result, there is an increasing need for efficient resource utilization and process intensification across various industries.[3,4] One key aspect of achieving this efficiency lies in understanding gas–liquid multiphase flow and its applications in industries such as power, coal, metallurgy, petroleum, chemical.[5,6] For example, in the plate distillation columns in the chemical industry, the rising vapor bubbles pass through the liquid layer, facilitating mass transfer with the liquid phase, which is closely related to tower efficiency.[7,8] Therefore, studying gas–liquid two-phase flow and bubble characteristics is of significant importance and has attracted increasing attention from both industry and academia.[9]

In industrial applications, bubbles are generated to enhance the interphase heat and mass transfer rates. Bubble characteristics, such as size, rise velocity, and trajectory of bubbles, play an essential role in heat and mass transfer process.[10,11] A comprehensive understanding of single bubble motion behavior can provide a foundation for studying multi-bubble motion, bubble group motion, and bubble motion in industrial devices.[12,13] Various factors such as liquid phase characteristics, initial bubble diameter, and mass transfer processes can have an impact on single bubble motion behavior.[14,15] Tripathi *et al.*,[16] and Sharaf *et al.*[17] charted new territory in understanding bubble dynamics through extensive experiments and simulations. They revealed bubble behavior over a wide range of Galilei and Eotvos numbers, a first in the field. This novel research identified two unique bubble breakup modes, establishing a strong link between shape asymmetry and path instability. The work of Sahu's team offers an invaluable cornerstone for further research in multiphase flows, leaving an indelible mark on the scientific community. Their efforts illuminate the complexities of bubble behavior, enriching our knowledge of this intriguing phenomenon. Liu *et al.*[18] captured the trajectory of bubbles during ascent by using PIV (Particle Image Velocimetry). They found that bubbles in high-viscosity liquids rose straight up; in medium-viscosity liquids, the bubble initially rose in a straight line and then changed to a "Z" path

after reaching a certain height.[19,20] In low-viscosity liquids, bubble trajectories were spiral, while the bubbles themselves rotated and wobbled.[21,22] Wu and Gharib[23] discovered that when the bubble diameter ranged from 0.15 to 0.25 cm, the bubble cross section had two stable shapes: spherical and elliptical. For spherical bubbles, when the bubble diameter exceeded 0.19 cm, the motion path becomes zigzag. For elliptical bubbles, when the diameter was larger than 0.21 cm, the rising path is spiral.[24,25]

Different bubble shapes may affect the flow pattern of the fluid surrounding the bubble. Researchers have summarized bubble shapes at different dimensionless numbers,[26,27] describing a total of five types of bubbles: spherical, elliptical, spherical-cap, skirted, and concave elliptical-cap shapes.[28,29] Funfschilling and Li[30] investigated the flow fields around bubbles in Newtonian and non-Newtonian fluids and demonstrated that flow fields around bubbles differed to some extent. Zhang *et al.*[31] studied flow fields surrounding moving bubbles in shear-thinning fluids with flow properties, finding that the flow properties around the bubble field gradually deviated from those in Newtonian fluid as the shear-thinning properties became more pronounced. Premlata *et al.*[32] examined different flow patterns inside a regularly shaped bubble. Li *et al.*[33] simulated the rising behavior of a single bubble at different pressures, revealing the vortices and wake vortices generated by the bubble motion.

As demonstrated above, although some research has been conducted, a thorough analysis of single bubble motion behavior remains limited, and the mechanism of bubble deformation under the flow field both outside and inside the bubble requires further examination.[34,35] In this work, the flow and fluid behavior of a single bubble were numerically simulated and experimentally investigated, with simulation results validated against experimental data. The bubble motion, bubble shape, and internal flow field of bubble were comprehensively studied under four different initial diameter bubbles and various concentrations of glycerol solutions to analyze the flow pattern within multiple bubble forms.

## II. SINGLE BUBBLE FLOW: EXPERIMENTAL AND NUMERICAL CALCULATION SCHEME

### A. Experimental systems and solutions

The layout of the entire experimental system is depicted in Fig. 1. The rectangular tank is made of a high-definition acrylic sheet with dimensions of $400 \times 200 \times 400\ \text{mm}^3$. The liquid level is maintained at a constant height of 300 mm during the experiments, with water and various concentrations of industrial glycerin used as the liquid medium. The viscosity and surface tension coefficients of different liquids were measured using a viscometer and surface tension meter with the physical parameters shown in Table I at 21 °C. An adjustable air volume air pump generates individual bubbles periodically, with nozzles fixed at the tank's bottom. The initial bubble size can be adjusted by changing the nozzles to different diameters. The experimental nozzles have outlet diameters of 2, 4, 6, and 8 mm, respectively, with identical structural parameters except for different outlet diameters. The image capture system is based on a particle image velocimetry system (TSI Particle Image Velocimetry, USA). According to experimental needs, the light source was replaced by an LED backlight from a laser generator, with the LED light source positioned at the tank's backside and supplemented by a diffuser plate to produce a more uniform backlight. A high-resolution interframe CCD camera (633 059 4MP) photographs the moving bubbles.

### B. Simulation model and numerical setup

#### 1. Control equations and solution method

The numerical model employs a set of control equations for the entire computational domain, considering surface tension and physical

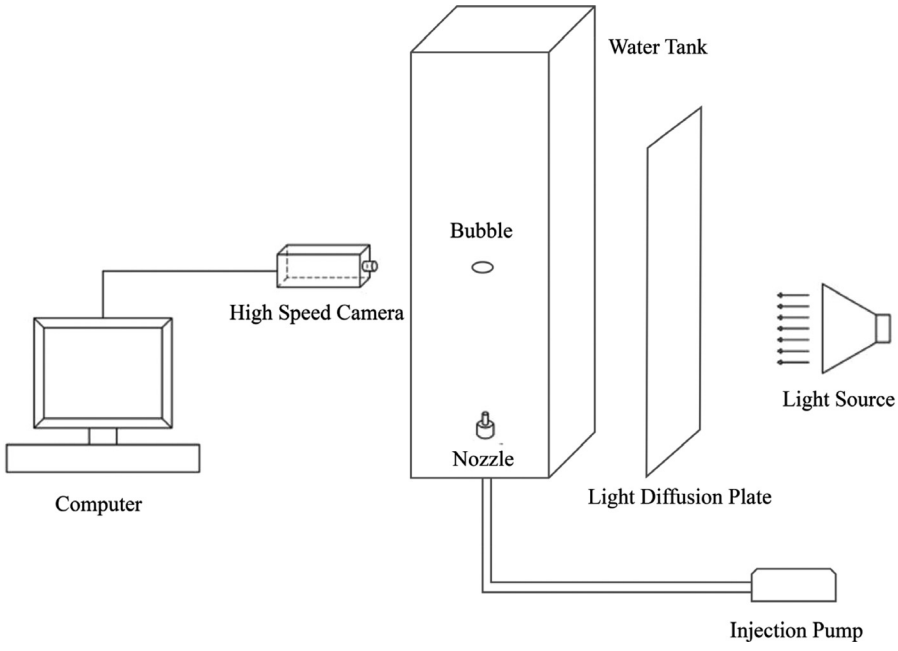


FIG. 1. Diagram of the bubble visualization experimental setup.

**TABLE I.** Physical parameters of different glycerol solutions.

| Fluid | $\rho$ (kg m$^{-3}$) | $\mu$ (kg m$^{-1}$ s$^{-1}$) | $\sigma$ (N m$^{-1}$) |
|---|---|---|---|
| Water | $0.998 \times 10^{3}$ | $1.01 \times 10^{-3}$ | $7.28 \times 10^{-2}$ |
| 30 wt. % glycerol | $1.047 \times 10^{3}$ | $1.87 \times 10^{-3}$ | $7.09 \times 10^{-2}$ |
| 70 wt. % glycerol | $1.153 \times 10^{3}$ | $1.43 \times 10^{-2}$ | $6.77 \times 10^{-2}$ |
| 100 wt. % glycerol | $1.256 \times 10^{3}$ | $7.99 \times 10^{-1}$ | $6.53 \times 10^{-2}$ |

properties variations. Assuming that the fluid motion is governed by the incompressible Navier–Stokes equations and the continuity equation, a surface-tracking model with a fixed volume-of-fluid (VOF) grid is used to determine the interface location between multiple mutually immiscible fluids.[36,37] In this model, the fluids share a momentum equation, and each fluid's volume fraction is traced inside each grid, with the gas and liquid phases following the continuity and momentum equations as shown in Eqs. (1) and (2), respectively,

$$\nabla \cdot \mathbf{u} = 0, \tag{1}$$

$$\frac{\partial(\rho \mathbf{u})}{\partial t} + \nabla \cdot (\rho \mathbf{u}\mathbf{u}) = -\nabla p + \nabla \cdot \left[\mu(\nabla \mathbf{u} + \nabla \mathbf{u}^{T})\right] + \rho g + F_s, \tag{2}$$

where u is the velocity vector, $\rho$ is the density, p is the pressure, $\mu$ is the viscosity, and $F_s$ represents the surface tension source term. The continuous surface force (CSF) model accomplishes this by converting the surface tension into a volume force acting on the interface based on the scattering theorem.[38] The resulting surface tension source term in the momentum equation is shown in Eq. (3), where $\sigma$ is the surface tension.

$$F_s = \sigma \frac{\rho \kappa \nabla \alpha}{0.5(\rho_1 + \rho_2)}. \tag{3}$$

A pressure-based non-stationary implicit solver is chosen to solve the equations. The volume fraction-related parameters are calculated using an explicit formula, with the Courant number set to 0.25. The Courant number is the number of meshes a fluid mass can cross in a time step, and the larger the time step, the larger the Courant number.[39,40] It is calculated as follows:

$$\text{Courant number} = \frac{u \Delta t}{\Delta x}, \tag{4}$$

where u is the flow rate, $\Delta t$ is the time step, and $\Delta x$ is the grid size. In general, a large Courant number may lead to computational dispersion, while a small Courant number signifies a high computational cost.[41,42] The momentum equation is discretized using the second-order upwind method, and the pressure is interpolated through the PRESTO! method, which calculates the "staggered" pressure using a discrete continuum balance of staggered control bodies on a surface method. The coupling method for pressure and velocity employs the PISO algorithm, primarily developed for the SIMPLE series of algorithms in which the momentum equation and mass continuity equation corrections are not synchronized. The main idea is to introduce a velocity correction step after the pressure correction step in the SIMPLE algorithm, ensuring that the iterative equation explicitly satisfies mass conservation while implicitly fulfilling momentum conservation. This equation can enhance the computational efficiency.

### 2. Determination of the calculation basin and selection of variables

In this study, we primarily employ the fluent VOF multiphase flow model to analyze the motion of buoyant bubbles in liquids with varying viscosities. Figure 2 displays a schematic diagram of the calculation domain, which features an initial bubble diameter of 2 mm, an initial position 20 mm above the bottom, and an initial water level height of 300 mm, consistent with experimental conditions. The initial circular bubble is positioned at the bottom of the computational flow field, and its upward motion is driven by buoyancy. No-slip wall boundary conditions are applied to the sides and bottom of the domain, while the top is setup as a pressure outlet that only allows water return, with gravity effects considered throughout the simulation. The experiments in this study utilize a single camera to capture instantaneous bubble images, focusing on bubble deformation and motion behavior, thereby reducing the model to a two-dimensional problem for study and simplification. The flow field surrounding bubbles of different initial diameters, the change in bubble shape in glycerol solutions of varying concentrations, and the alteration of flow patterns inside the bubbles are primarily investigated. We analyze the flow pattern inside the bubble with various forms, conduct numerical calculations using fluent hydrodynamic software, and initially assume the liquid to be stationary in the simulation.

In previous research, bubbles were continuously released from the bottom injection port.[17] In the present simulation, the liquid was initially assumed to be stationary. Four glycerol–water mixtures with distinct physical properties served as the liquid phase in the simulations, while the rising motion of bubbles with initial diameters of 2, 4, 6, and 8 mm was investigated. Various physical parameters of glycerol solutions with different concentrations vary, particularly viscosity, which increases tenfold as glycerol concentration rises. Consequently, the study of the motion behavior of individual bubbles in distinct liquid-phase environments essentially investigates the influence of liquid-phase viscosity on bubble shape and flow field flow conditions.

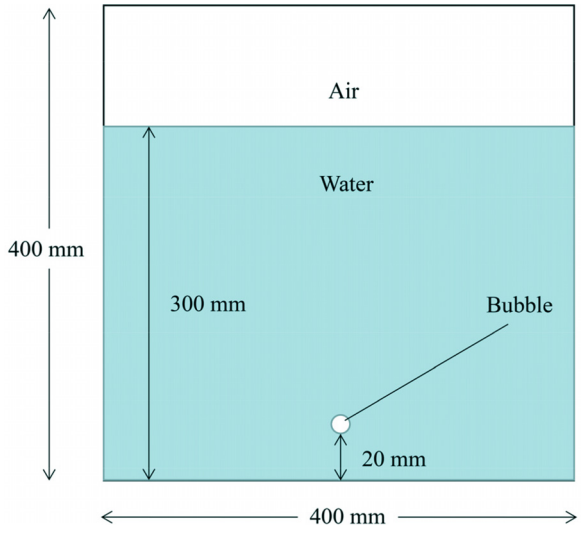


**FIG. 2.** Schematic diagram of the computational domain used to simulate the rise of bubbles in a liquid.

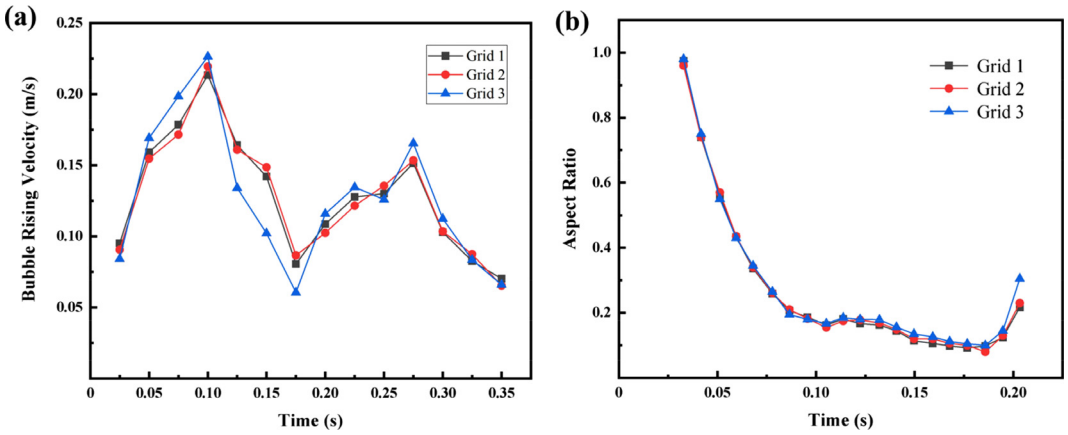


**FIG. 3.** Bubble rise rate (a) and deformation ratio (b) for the three grid scenarios.

### 3. Grid irrelevance test

The grid-independence test evaluates the effect of the grid on the computational results and strikes a balance between computational accuracy and cost by selecting an appropriate grid size. Typically, this test involves selecting one or two variables that best reflect the simulation situation in numerical calculations, and comparing the calculation results under different grid sizes to determine the optimal grid. In our study, we employed three different grid schemes with varying sizes and assessed their influence on the results. Given the small size of the flow field calculation area and the need for accurate flow field condition calculations during bubble deformation and flow pattern changes, inside the bubble, the sizes of the three schemes are set to relatively small values. The three grid size schemes used were as follows: scheme I ($0.4 \times 0.4\,mm^2$), scheme II ($0.5 \times 0.5\,mm^2$), and scheme III ($0.6 \times 0.6\,mm^2$). The simulation of the bubble rise process in a 30 wt. % glycerol solution was performed to examine the dependence of the simulation results on grid resolution.

The grid-independence test focused on the rising speed of the bubble during its ascent, revealing that the three grid schemes with different sizes provide better numerical calculation results in terms of grid size and number.

The calculation results of the three grid schemes are illustrated in Fig. 3. Regarding the rising rate of the bubbles, schemes 2 and 3 display a slight deviation between 0.2 and 0.3 s but remain largely consistent. In contrast, schemes 1 and 3 reveal a considerable deviation between 0.1 and 0.175 s, especially at 0.125 s, where the deviation is the largest. As for the bubble deformation ratios, the three grids are nearly identical up to 0.1 s. After 0.1 s, scheme 3's results diverge more than those of the other two grid schemes and exceed the data from the other schemes. By comparing the bubble rise rates and deformation ratios for the three scenarios, it becomes evident that the 63 441 grid in scheme 2 more closely aligns with the 93 689 grid in scheme 3, while the 45 952 grid in scheme 1 strays from scheme 3. This enables a reduction in computation expenses while minimizing the grid's influence on the calculated outcomes. As a result, the grid size of scheme 2 is selected.

### 4. Computational model validation

The computational model validation is achieved by comparing the calculated and experimental results. In this study, the initial shape of the bubbles is spherical, so the optimal condition for comparison in the experiment is for the bubbles to assume a spherical shape after they have been released from the injection device. High-speed photography records the motion of the bubbles in the experimental setup, and the deformation ratios of the bubbles are compared based on their specific shapes. Two different liquid-phase environments, water and 70% glycerol solution, were selected to compare the results at different viscosities.

Table II presents the comparison between the experimentally observed bubble deformation ratios in water and the numerically calculated values, while Table III displays the comparison for the 70% glycerol solution. The results reveal that the maximum error between the two at 20 ms is 7.8% for bubbles in water, with the relative error ranging from 2.1% to 5.4% for 10, 20, 30, and 40 ms, respectively. The maximum relative error of 7.8% falls within a reasonable range for flow field calculations.

For bubbles in the 70% glycerol solution, the maximum error between the two is 5.4% at 20 ms. When comparing the results for 5, 10, 20, 30, and 40 ms, the relative error varies between 1.5% and

**TABLE II.** Comparison between experimental and numerical values of bubble deformation ratios in water.

| | 5 ms | 10 ms | 20 ms | 30 ms | 40 ms |
|---|---|---|---|---|---|
| Experiment | 0.945 | 1.036 | 1.156 | 1.321 | 1.529 |
| Numerical calculation | 0.986 | 1.058 | 1.246 | 1.375 | 1.611 |
| Relative error (%) | 4.3 | 2.1 | 7.8 | 4.1 | 5.4 |

**TABLE III.** Comparison between experimental and numerical values of bubble deformation ratios in 70% glycerol solution.

| | 5 ms | 10 ms | 20 ms | 30 ms | 40 ms |
|---|---|---|---|---|---|
| Experiment | 0.923 | 0.975 | 1.021 | 1.086 | 1.112 |
| Numerical calculation | 0.941 | 1.009 | 1.076 | 1.102 | 1.146 |
| Relative error (%) | 2.0 | 3.5 | 5.4 | 1.5 | 3.1 |

3.5%. The maximum relative error of 5.4% is also within a reasonable range for flow field calculations. In conclusion, the calculation method employed in this study demonstrates a high degree of accuracy.

While the deformation ratio calculation results are satisfactory, this study necessitates a focus on the specific bubble shape. Consequently, the deformation ratio alone is insufficient to demonstrate the calculation's effectiveness. A comprehensive validation of the results requires comparing the numerically calculated bubble shape and rise path with the experimentally captured results.

Figure 4 presents a comparison between the experimentally observed bubble shape and the rise path at different time instances under experimental conditions featuring an initial diameter of 4 mm in water. To mitigate the possibility of experimental inconsistencies, several trials were conducted under these specific conditions. As can be seen from the figure, the initial round bubble gradually transitions to an oval shape as it ascends. This confirms that the calculation model employed in the numerical calculation can yield more accurate calculations.

## III. RESULTS AND DISCUSSION

### A. Flow field variation around bubbles in different gas–liquid systems

Buoyancy drives bubbles to rise in a liquid, with bubble motion characteristics (bubble shape and rising speed) significantly influenced by the liquid's viscosity.[43,44] The motion of bubbles impacts the surrounding fluid flow, affecting convective mass transfer and the liquid's flow state. The mass transfer process is primarily influenced by the main body of the flow, i.e., the effect of bubble movement. Therefore, analyzing the fluid flow around the bubble serves as the basis for studying the motion of numerous bubbles and the mass transfer process in the industrial production. The fluid flow around the bubble can be characterized by the Reynolds number (Re), calculated as follows:

$$\mathrm{Re} = \frac{D \times U \times \rho}{\mu}, \tag{5}$$

where $D$ is the bubble diameter (m), $U$ is the bubble rise velocity (m/s), $\rho$ is the density (kg/m$^3$), and $\mu$ is the viscosity (Pas), the Re number ranges from 259 to 1952. Figure 5 shows the velocity vector diagram of the flow field around the bubble in water, with colored arrows indicating the flow direction of the liquid. In the initial stage of bubble rise, bubbles and trails exhibit axisymmetric and slow movement, as seen in Figs. 5(a) and 5(b). The liquid flow around the bubble covers a small range, forming a pair of vortices on both sides of the bubble. As the bubble rises, its rise speed accelerates, and the volume of the liquid being entrained in the flow around the bubble increases [Figs. 5(c)–5(f)]. The wake symmetry gradually breaks, and the bubble wake vortex detaches and changes direction [Figs. 5(e) and 5(f)]. The amount of liquid being entrained in the flow below the bubble is significantly greater than that above the bubble, which is because the liquid at the top of the bubble remains relatively static when no bubble has passed through. In contrast, the liquid at the bottom, due to the bubble's rise, generates an instantaneous void and pressure difference, resulting in the surrounding fluid to fill these vacancies and create a larger flow. The faster the bubble rises, the stronger the perturbation of the surrounding fluid, and the longer the motion trails at the bottom of the bubble, generating vortex.

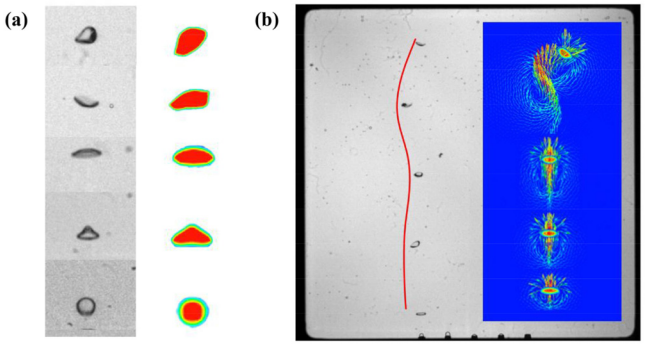


**FIG. 4.** Experimental filming of bubble shape change (a) and rise path (b) compared to numerical calculations.

Figure 6 shows the velocity vector diagram of the flow field around the bubble in a 30% glycerol solution, the Re number ranges from 138 to 894. Similar to bubbles in water, the rising velocity of the bubble generally increases as it ascends through the liquid. Concurrently, the volume of liquid set in motion beneath the bubble progressively expands, and it is notably larger than the volume of liquid set in motion above the bubble. Comparing Fig. 6 with Fig. 5 reveals that the motion trails in the lower part of the bubble are longer and exhibit a higher degree of curvature. In this flow field, the vertical distance the bubble rises increases, and the oscillation amplitude in the x direction of the bubble decreases compared to Fig. 5.

Figure 7 shows the velocity vector diagram of the flow field around the bubbles in 70% glycerol solution, and the Re number ranges from 16 to 161. The viscosity of 70% glycerol solution significantly increases compared to water and 30% glycerol solution, and the rising velocity of its bubbles decreases considerably. In Fig. 7, the length of the bubble motion wake increases significantly, and the vortex position at the ends of the bubble gradually moves downward as the bubble rises.

Comparing Figs. 5 and 6, the bubble oscillates less in the x direction throughout the rise, and the increased liquid viscosity causes the distance from the bubble itself to the tail vortex detachment on both sides of the bubble to become smaller. This reduces the bubble's horizontal movement distance and decreases the disturbance of the bubble to the fluid. As the viscosity increases again, this effect may become more pronounced, so the flow field in 100% glycerol was further examined.

In 100% glycerol solution, the Re number of most of the bubbles is between 3 and 17. At this stage, the viscosity of the liquid is high, causing the bubbles to form in a consistently spherical shape. As expected, the increase in the liquid's viscosity further reduces the bubbles' rising velocity to a velocity of $10^{-2}$ steps m/s. The fluid flow surrounding the bubble remains stable, and there is no significant change in the vortex positions at both ends. Upon comparing the glycerol–water mixture solutions with different physical properties, it is evident that the bubble rises in a straight line without any deviation. No vortex is present in the wake below the bubble, and only a symmetrical pair of vortices exists at both ends of the bubble.

Figure 8 shows the trend of the oscillation amplitude in the X direction during the rise of bubbles in different liquid phase

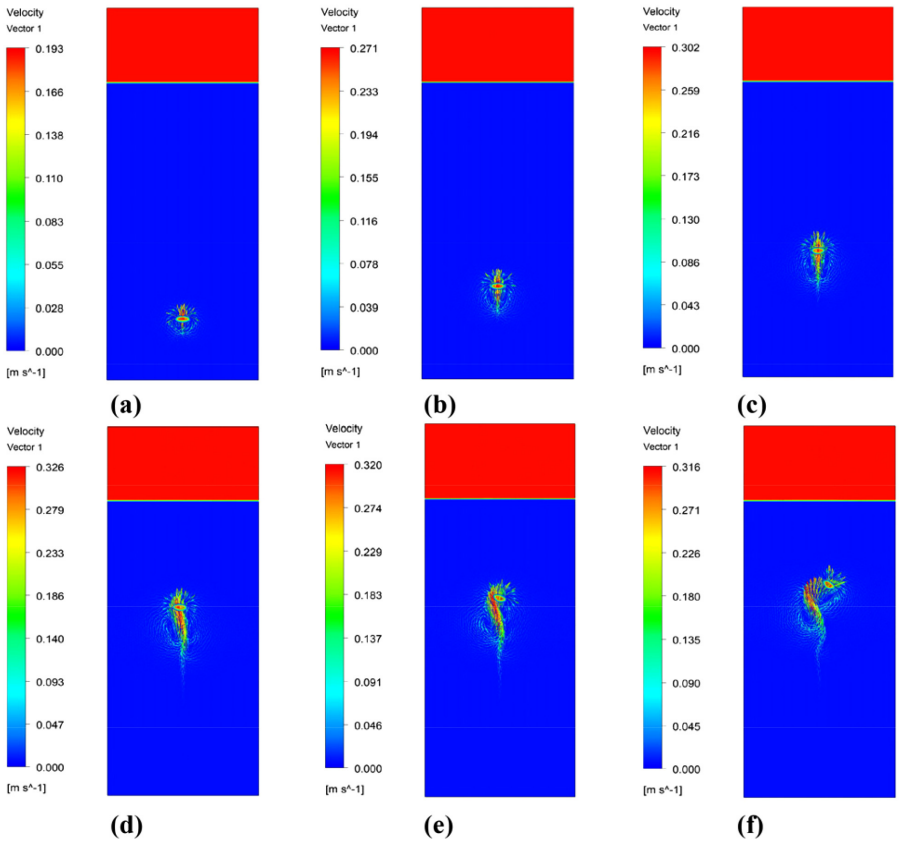


**FIG. 5.** Velocity vector diagram of the flow field around the bubble in water: (a)–(f) bubble at different moments.

environments, where the oscillation amplitude value indicates the distance of the bubbles from the nozzle center axis in the X direction during the rise. As the viscosity of the liquid increases, the amplitude of oscillation in the X direction decreases for bubbles of the same diameter during the ascent process. The maximum amplitude of oscillation in the X direction in water was 3.8 mm, in 30% glycerol solution the maximum amplitude of oscillation in the X direction was 2.3 mm, and in 70% glycerol solution the maximum amplitude of oscillation in the X direction was 0.73 mm. In 100% glycerol, the maximum X-direction oscillation amplitude was only 0.13 mm, which is significantly lower than those in 70% glycerol solution, 30% glycerol solution, and water.

Within the same liquid phase, the X-direction oscillation amplitude notably increases with the initial diameter of the bubble. In the case of water, the maximum X-direction oscillation amplitude is 0.63 mm for 2 mm bubbles, 0.8 mm for 4 mm bubbles, and 1.9 mm for 6 mm bubbles. The maximum X direction oscillation amplitude for the 8 mm bubble was 3.8 mm.

### B. Bubble trajectory under different gas–liquid conditions

The trajectory of the bubbles under various working conditions was charted by capturing instantaneous images of the bubbles at different moments during their ascent, as illustrated in Fig. 9. In water, when a bubble detaches from the nozzle, its shape rapidly changes from spherical to flat ellipsoidal, and then to various shapes such as ball-cap and mushroom due to surface oscillations. At a 2 mm diameter, the bubble trajectory is closer to a straight line. As the initial diameter of the bubble increases, the fluctuations in the x direction of the bubble trajectory increase, resulting a zigzag pattern.

In the 70% glycerol solution, the bubbles primarily maintain a spherical or ellipsoidal shape after leaving the nozzle and remain relatively constant during their ascent. When the bubble diameter is 2 mm, the bubble shape is almost spherical. As the nozzle outlet diameter increases, the bubble shape becomes more ellipsoidal and flatter, meaning that the bubble aspect ratio decreases as the initial diameter grows. As shown in Figs. 9(e)–9(h), the bubble trajectories are all approximately straight lines, with only minor fluctuations in the x direction at bubble diameters of 6 and 8 mm, in contrast to Figs. 9(a)–9(d). It is evident that the rising trajectory and morphological changes of the bubbles are highly dependent on the properties of the liquid, particularly its viscosity. High viscosity inhibits bubble deformation and restricts lateral movement. The viscosity of pure glycerol is quite high, causing a significant reduction in bubble rising velocity to $10^{-2}$ m/s. The surrounding liquid flow is more stable, resulting in uniformly spherical bubbles that rise in a straight path without deviation.

The process of bubble formation and detachment from the nozzle significantly influences the subsequent bubble development. The physical properties of the 70% glycerol solution used in this experiment are more general and representative compared to those of the

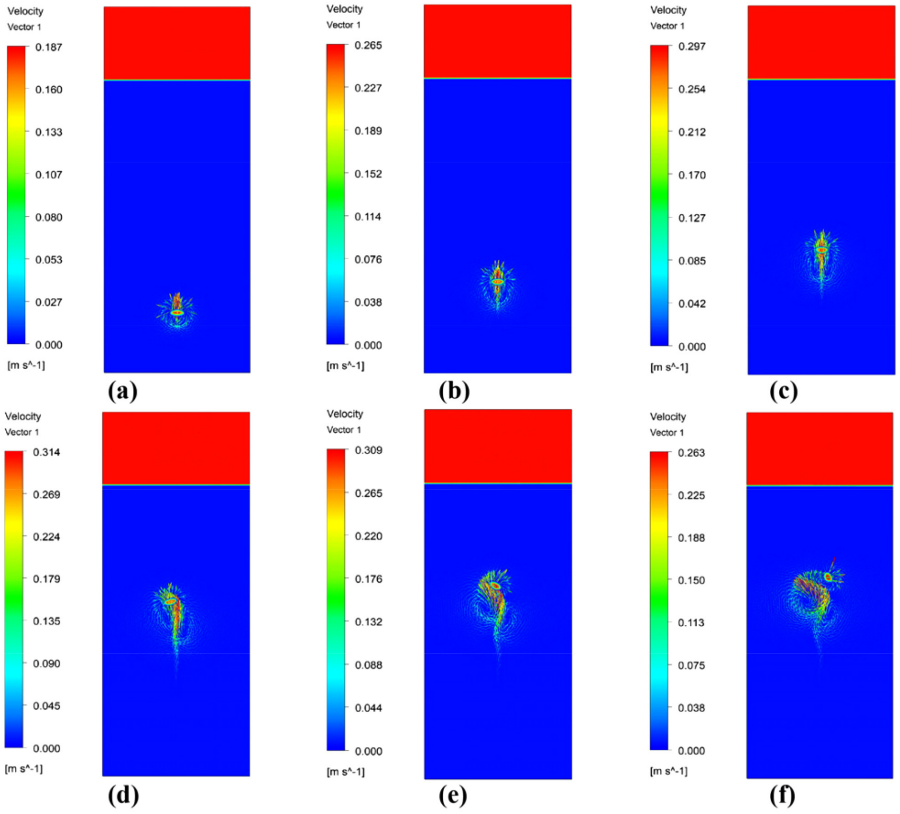


**FIG. 6.** Velocity vector diagram of the flow field around the bubble in 30% glycerol solution: (a)–(f) bubble at different moments.

30% and 100% glycerol solutions. Therefore, we separately analyzed the morphology and characteristics of bubble detachment from the nozzle in water and 70% glycerol solutions. Figure 10 presents the bubbles generated when gas is injected into the 70% glycerol solution, capturing the moment of detachment from the nozzle outlet at various sizes. In contrast, Fig. 11 depicts the bubbles at the moment of release from the nozzle in water. The comparison reveals that all bubble patterns are axisymmetric, with the nozzle outlet's central axis as the reference, indicating that the horizontal forces remain in equilibrium during the bubble formation process. Within the same liquid, the overall height and width of the bubbles increase as the nozzle diameter expands. Simultaneously, the neck between the bubble and the nozzle lengthens as the nozzle outlet diameter grows.

After the gas flows through the nozzle, the bubble shape approaches a spherical form due to surface tension. Since the bubble has not yet exited the nozzle at this stage, the continuous injection of air causes the bubble's volume to gradually increase, maintaining a balance between surface tension and the resistance of the surrounding liquid. When the nozzle outlet diameter remains constant, the bubbles generated in water exhibit greater overall height and width compared to those in the 70% glycerol solution, and this pattern holds true across different nozzle sizes.

In earlier studies, the characteristics of bubbles detaching from the nozzle in liquid nitrogen and water were investigated. Despite the substantial difference in surface tension between the two liquids, the experimental results revealed minimal differences in the equivalent diameters of the bubbles at the instant they detached from the nozzle. This finding suggests that surface tension has a significantly smaller impact on bubble size than liquid viscosity during the bubble formation phase.

### C. Variation of bubble shape in different gas–liquid systems

The bubble shape changes during its motion. Bubble deformation states and deformation ratios were investigated during the rising motion of bubbles with initial diameters of 2, 4, 6, and 8 mm under different gas–liquid systems. The deformation ratio $A_r$, calculated as the ratio of the longitudinal projection length of the bubble to its transverse projection length, is as follows:

$$A_r = \frac{d_v}{d_h}, \tag{6}$$

where $d_v$ is the longitudinal projection length of the bubble and $d_h$ is the transverse projection length of the bubble.

Figure 12 displays the shape changes during the rise of the four initial diameter bubbles in the water–air system, becoming more dramatic as the initial diameter of the bubbles increases. When the initial diameter of the bubble is 2 mm, the round bubble first transforms into an ellipse and progressively flattens. After 0.15 s, both bubble ends gradually rise, with minimal overall change. For 4 mm initial diameter, the bubble initially adopts a ball-cap shape, with the lateral length

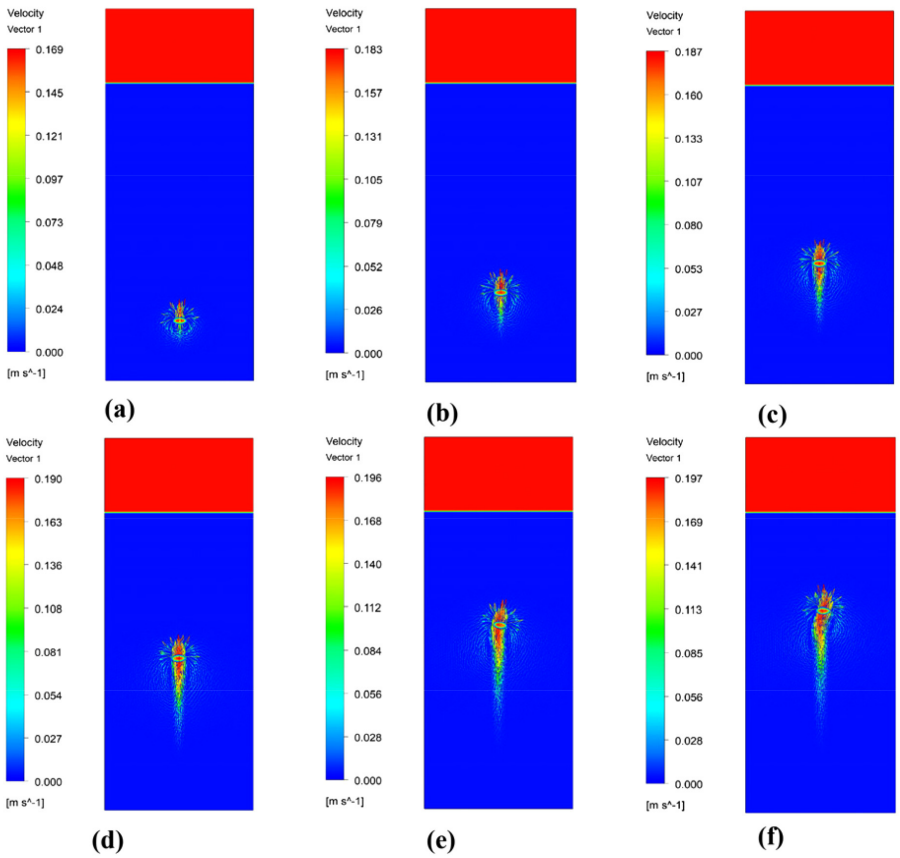


**FIG. 7.** Velocity vector diagram of the flow field around the bubble in 70% glycerol solution: (a)–(f) bubble at different moments.

increasing. After 0.175 s, the bottom of the bubble slightly depresses, and the middle section slightly convex upward, further compressing the longitudinal dimension, transitioning to a flatter shape. The 2 and 4 mm bubbles differ in shape, but their transformations remain symmetrical. However, as the initial diameter increases to 6 and 8 mm, the bubble transitions from spherical to an almost circular cap shape before 0.1 s. The bubble ends then extend downward, assuming an elliptical cap shape. As the bubble rises, the bottom depression evolves into a skirt, increasing in size over time. After 0.2 s, the trend of bubble morphology changes decreases to an upper semi-elliptical shape. A comparison of bubble patterns captured with the high-speed camera in this experiment found consistency with numerical simulation results.

Figure 13 illustrates the deformation ratio trends for bubbles of different diameters in various liquid-phase environments. In Fig. 13(a), the deformation ratio variations for bubbles in the water–air system are depicted. For the 2 and 4 mm bubbles, the deformation ratio initially decreases until 0.175 s before experiencing a slight increase. This is attributed to the bubble ends curving upward, resulting in an increased longitudinal projection length. For larger diameter bubbles, the deformation ratio tends due to more pronounced deformation.

In the 30% glycerol solution–air system, bubble deformation resembles the overall shape change trend observed in the water–air system, albeit with less pronounced changes. Thus, the shape change during the rise of four initial diameter bubbles in the 70% glycerol solution–air system is directly analyzed, as shown in Fig. 14. The 2 mm initial diameter bubble changes from spherical to elliptical at the start of its ascent, maintaining this shape throughout. The deformation ratio of the 4 mm bubble shifts from 0.87 to 0.66, and its shape becomes flat after 0.2 s, differing from the anti-sphere cap shape observed in the water–air system. Additionally, the 6 and 8 mm bubbles still exhibit significant deformation. After 0.2 s, bubbles of varying initial diameters reach a stable shape. For small diameter 2 mm bubbles, the final shape is elliptical, whereas the 6 and 8 mm bubbles attain an elliptical and ball-cap shape. The experimental bubble shape change from round to final ellipse closely resembles the bubbles in Fig. 14, indicating that the adopted theoretical model and the simulations results align with the experimental results.

Generally, for 2-mm-diameter bubbles, the deformation ratio change in 70% glycerol is smaller than in water, and the bubble shape in 70% glycerol is more stable than that in 30% glycerol solution and water. However, for larger bubbles, the deformation ratio variation is greater. Figure 13(c) displays the bubble deformation ratio variation in this system. There is no major change in the deformation ratio for 2 mm bubbles, while the deformation ratio for larger diameter bubbles gradually decreases and stabilizes. The contrasting deformation ratio trends between small and large bubbles stem from differences in the liquid phase's physical properties, particularly viscosity. The density and surface tension differences between 70% glycerol and water are negligible, whereas the former's viscosity is 14.1 times greater than the

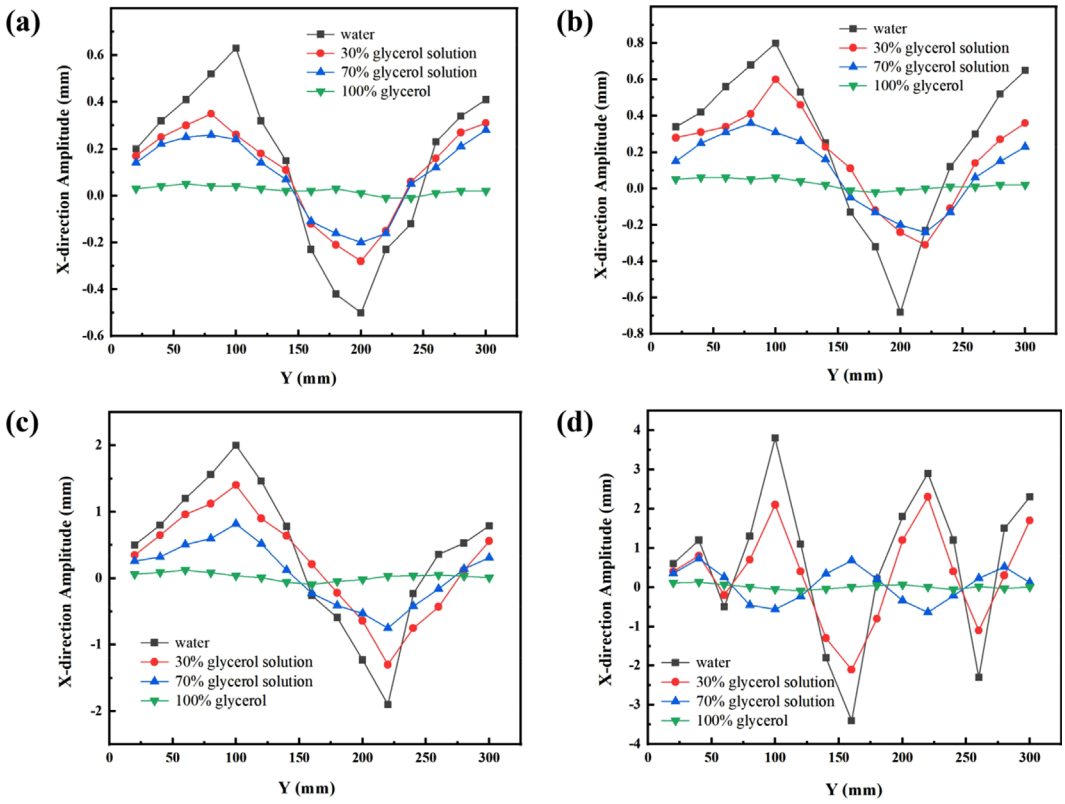


**FIG. 8.** Trend of oscillation amplitude in the x direction during the rise of the four gas–liquid systems: (a) 2 mm bubble; (b) 4 mm bubble; (c) 6 mm bubble; and (d) 8 mm bubble.

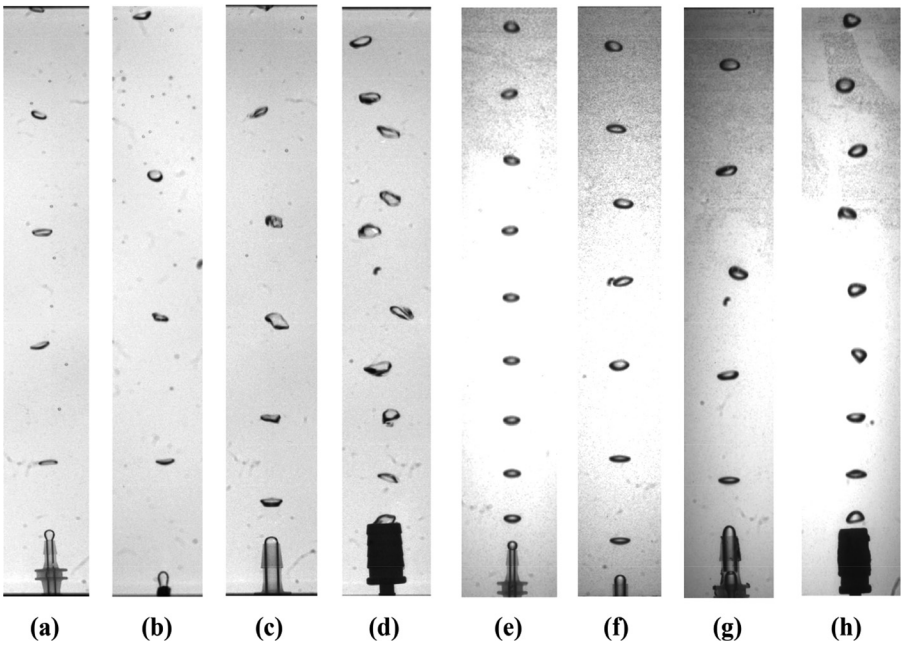


**FIG. 9.** Trajectory of bubble rise under different gas–liquid conditions (a) D = 2 mm, water; (b) D = 4 mm, water; (c) D = 6 mm, water; (d) D = 8 mm, water; (e) D = 2 mm, 70% glycerol; (f) D = 4 mm, 70% glycerol; (g) D = 6 mm, 70% glycerol; and (h) D = 8 mm, 70% glycerol.

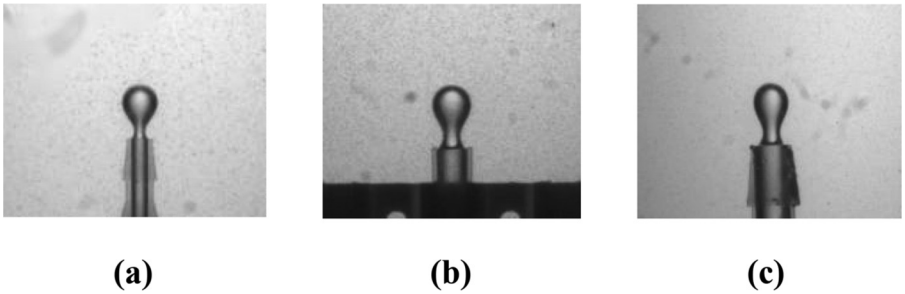


FIG. 10. Bubble shape at the moment of release from the nozzle in 70% glycerol solution (a) 2 mm bubble; (b) 4 mm bubble; and (c) 6 mm bubble.

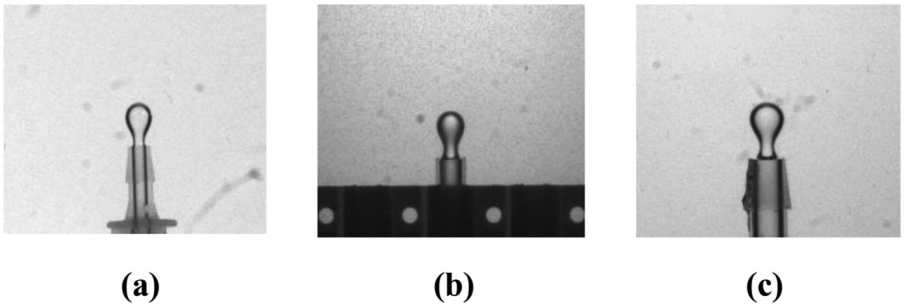


FIG. 11. Bubble shape at the moment of release from the nozzle in water (a) 2 mm bubble; (b) 4 mm bubble; and (c) 6 mm bubble.

latter. Consequently, viscosity, in addition to the initial diameter, is a major factor influencing bubble deformation. To further investigate viscosity's effect, a higher concentration glycerol solution was examined.

As depicted in Fig. 15, for the 100% glycerol solution–air system with a liquid phase viscosity of 799 mPa s, all bubble shapes experienced minimal change. Results obtained from both the present simulations and previous work indicate that,[17] unlike in other groups of gas–liquid systems, lateral flattening of the bubble shapes is minimal in this system. Figure 13(d) reveals that the deformation ratios of all bubbles are greater than 0.6, and for small bubbles, they are more stable than for large bubbles over a 0.25 s period. The larger the initial bubble diameter, the more stable and greater the deformation ratio. Moreover, in the 100% glycerol–air system, the range of deformation ratios for bubbles is significantly compared to other systems.

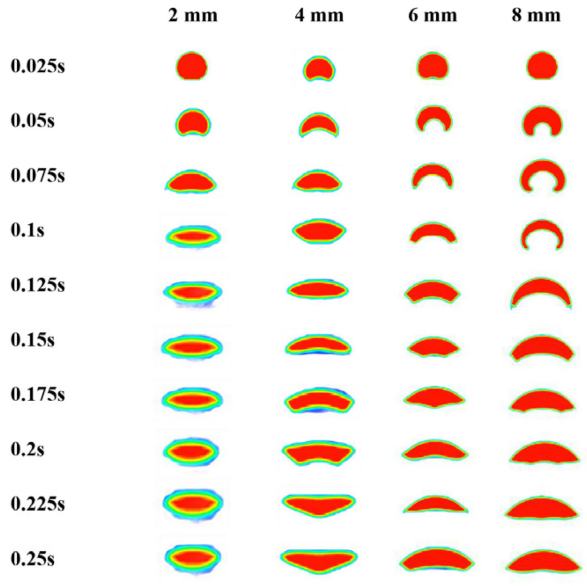


FIG. 12. The shape change of four different diameter bubbles in the water–air system during the rising process.

To further examine the impact of liquid viscosity and surface tension on bubble shape changes, the surface tension of water is used as a reference. Different magnitudes of liquid surface tension coefficients are set to simulate the bubble rising process under the ideal condition of maintaining constant liquid density and viscosity. Among common liquids, water has the largest surface tension, and inorganic liquids exhibit much greater surface tension than organic liquids. Figure 16 shows the shape change of a 6-mm-diameter bubble during its ascent in a liquid with a surface tension coefficient greater than that of water. When the surface tension is 0.05 N/m, the bubble extends downward at 0.075 s showing an elliptical cap shape at both ends. The depression at the bottom evolves into a skirt, and its size increases over time. After 0.15 s, the two ends of the bubble gradually warped upward and maintained their shape. At a surface tension of 0.3 N/m, the bubble initially transitions from a round shape to a ball-cap shape before oscillating between the ball-cap and anti-ball-cap shapes. As surface tension further increases, the overall shape fluctuation trend of the bubble decreases substantially. When the surface tension reaches 0.5 N/m, the perturbation of the fluid around the bubble during the rising process renders the bubble shape uneven and nearly circular. The bubble only exhibits minor longitudinal compression during the ascent. The increased surface tension continues to compress the

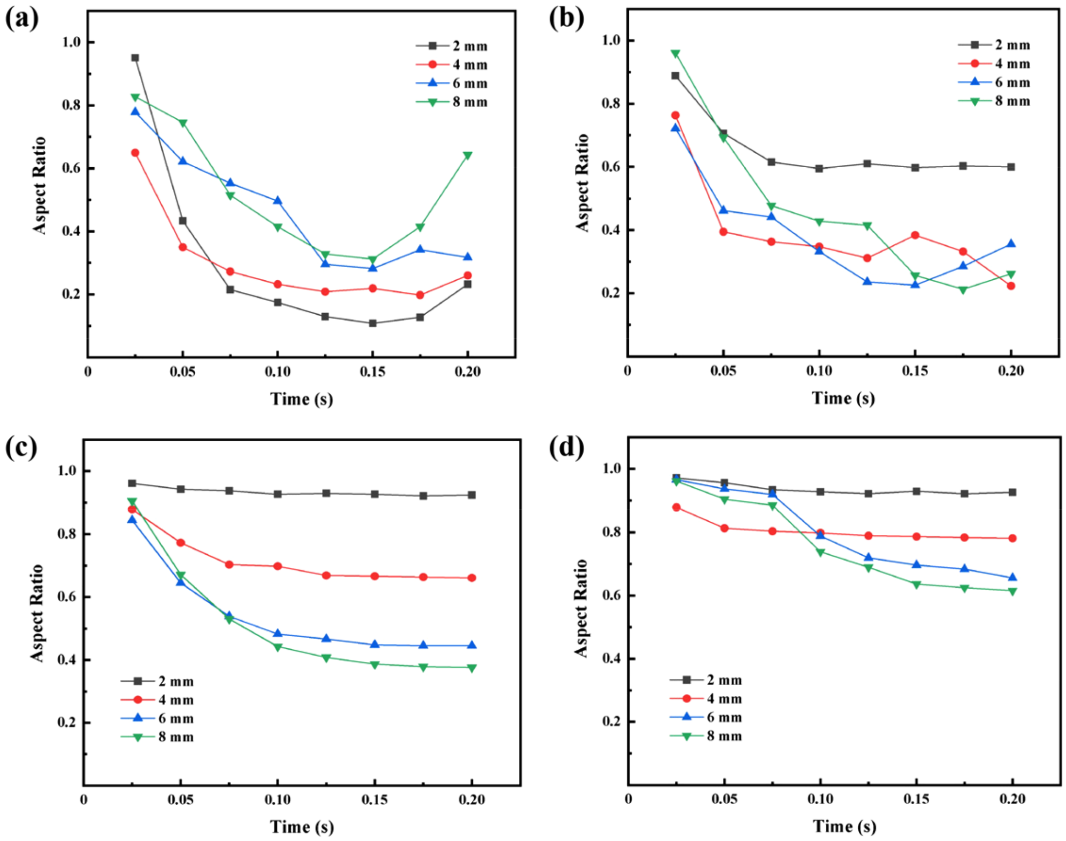


FIG. 13. Trend of bubble deformation ratios for different diameters in four gas–liquid systems: (a) water; (b) 30% glycerol solution; (c) 70% glycerol solution; and (d) 100% glycerol.

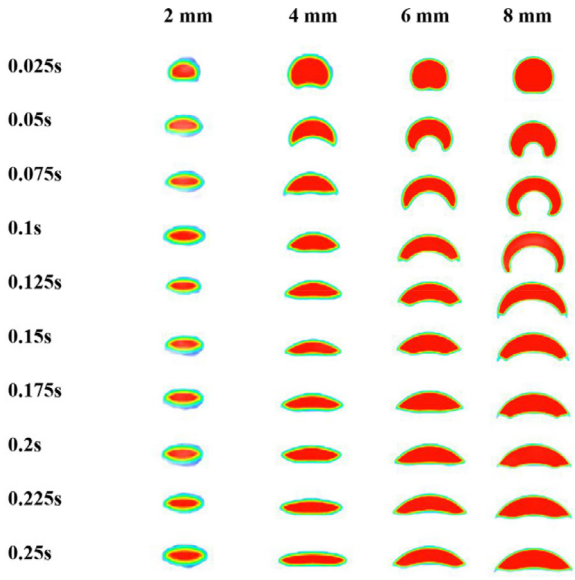


FIG. 14. Graph of shape change during the rise of four different diameter bubbles in the 70% glycerol solution–air system.

inhomogeneous part until it balances with other parts to restore equilibrium, causing the bubbles to display tilted fluctuations in space.

Figure 17 presents the shape change of 6-mm-diameter bubbles during their ascent in a liquid with a surface tension coefficient lower than that of water. It can be observed that the primary bubble splitting occurs during the ascent as the surface tension decreases with an order of magnitude trend. When the surface tension is 0.01 and 0.009 N/m, the bubble rapidly transitions from a round shape to a depressed outer skirt structure, and the bubble splitting at 0.15 s. The skirt structure to the left and right of the bubble detaches, forming two small bubbles. As the main bubble rises, the small bubble encounters resistance, causing the vertical distance between the small bubble and the main bubble to increase over time.

When the surface tension decreases to $10^{-4}$ N/m, an entirely unique situation arises, leading to the rupture of the main bubble at 0.075 s. The main bubble breaks into two symmetrical secondary bubbles, while the secondary bubbles further split into smaller bubbles both above and below, which tends to reduce energy (minimizing surface area), and when the surface tension is especially low, bubbles tend to increase their surface area. Consequently, small bubbles continue to break down, from two into three, three into four, until the bubble diameter becomes so small that it stops breaking. The comparative analysis reveals that when the surface tension of different liquids is

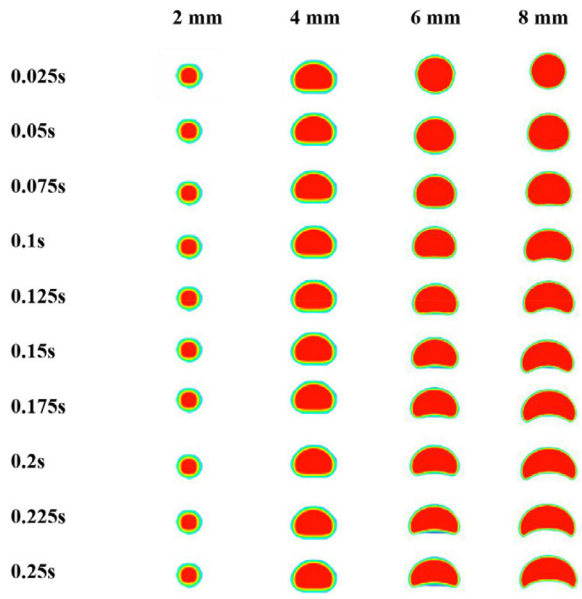


FIG. 15. Graph of shape change during the rise of four different diameter bubbles in the 100% glycerol solution–air system.

similar and the viscosity changes by an order of magnitude, the viscosity primarily affects the change in bubble shape. When the viscosity differences among different liquids are minimal and the surface tension changes by an order of magnitude, bubble deformation occurs but not rupture if the liquid surface tension is greater than $10^{-2}$ level N/m. If the liquid surface tension is less than $10^{-2}$ level N/m, the bubble ruptures the frequency of rupture increases as surface tension decreases.

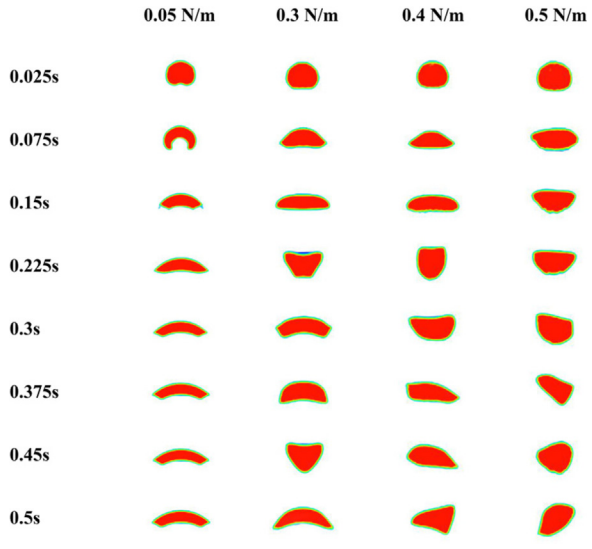


FIG. 16. Shape variation of bubbles of 6 mm diameter during their rise in a liquid with a surface tension coefficient greater than that of water.

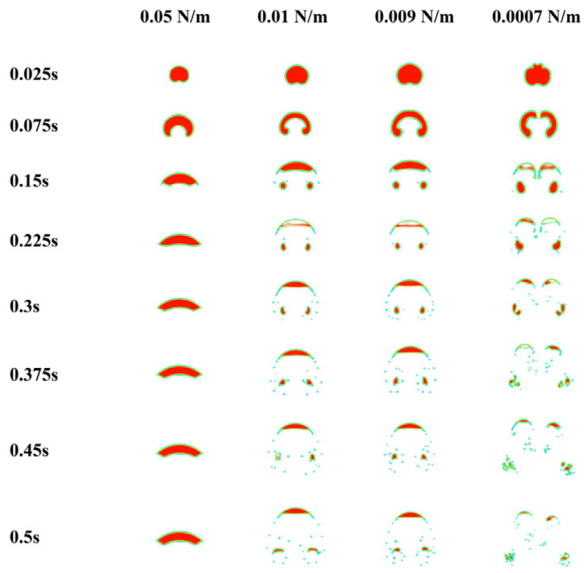


FIG. 17. Shape change of bubbles of 6 mm diameter during their rise in a liquid with a surface tension coefficient less than that of water.

## D. Analysis of the relationship between dimensionless numbers

### 1. Variation of the bubble deformation ratio Ar with Eo

The *Eo* number can be utilized to describe a bubble's shape within a moving fluid. It can be perceived as the ratio of buoyancy to surface tension and is expressed as follows:

$$Eo = \frac{\Delta\rho g L^2}{\sigma}, \tag{7}$$

where $\Delta\rho$ is the density difference between the liquid and the gas. Previous experiments have shown that the bubble shape is related to *Re* and *Eo*, with a large *Eo* being considered the main cause of bubble oscillation. Wellek *et al.* proposed a relationship between the bubble aspect ratio and *Eo*, as shown in the following equation:

$$A_r = \frac{1}{1 + 0.163 Eo^{0.757}}. \tag{8}$$

Based on the experimental results, it is known that *Eo* varies between 2 and 40. As *Eo* increases, the bubble deformation ratio exhibits a decreasing trend. At smaller *Eo* values, the deformation of the bubbles is relatively more pronounced, while a large deformation implies a larger bubble deformation ratio. Although the results obtained from the relational equation proposed by Wellek *et al.* were validated when the liquid medium was water, they were not as applicable when the viscosity of the liquid was further increased. Therefore, in this paper, Wellek's equation was modified based on experimental data of bubbles in 30%, 70%, and 100% glycerol solutions, respectively, and the modified equations are shown in the following equations:

$$A_r = \frac{1}{1 + 0.092 Eo^{0.721}}, \tag{9}$$

$$A_r = \frac{1}{1 + 0.075Eo^{0.724}}, \tag{10}$$

$$A_r = \frac{1}{1 + 0.061Eo^{0.743}}. \tag{11}$$

### 2. Variation of the bubble deformation ratio Ar with We

*We* is the ratio of inertial force to surface tension. The smaller the *We*, the more significant the role played by surface tension. The expression is as follows:

$$We = \frac{\rho v^2 l}{\sigma}. \tag{12}$$

The relationship between the aspect ratio *Ar* and *We* of the bubbles has been studied by several authors; for example, Wellek *et al.* gave Eqs. (13) and (14), respectively.

$$A_r = \frac{1}{1 + 0.091We^{0.95}}, \tag{13}$$

$$A_r = \frac{1}{1 + 5We/32}. \tag{14}$$

Figure 18 shows the data obtained from this experiment, where the gray scatter points represent those in water and the red scatter points are those in the 70% glycerol solution. For comparison purposes, both of these relationships are plotted together in the graph, as shown in the two curves. A comparison based on the data obtained in this experiment indicates that for bubbles in water, there is a good match with Taylor's equation. In contrast, for bubbles in higher-viscosity liquids, the equation proposed by Wellek aligns more closely with the experimental results.

### 3. Variation of the drag coefficient $C_D$ with Re

The drag coefficient plays an important role in the motion of bubbles and represents the relationship between liquid drag and inertial forces. Based on numerical simulations and experimental data, scholars have proposed various empirical formulas for the drag coefficient and obtained some research conclusions. Some scholars have also given the relationship equation between the drag coefficient and the Reynolds number. Kelbaliyev and Ceylan discussed the correlation between $C_D$ and Re and proved that the two dimensionless numbers are highly correlated.[45] This relationship was further refined by Turton *et al.* whose proposed equation for the relationship between $C_D$ and Re is given in the following equation:

$$C_D = \frac{24}{\mathrm{Re}}(1 + 0.173\mathrm{Re}^{1.657}) + \frac{0.413}{1 + 16\,300\mathrm{Re}^{-1.09}}. \tag{15}$$

From the experimental data, it can be concluded that in the 70% glycerol solution, the bubble Re was below 350 and the $C_D$ was between 2.3 and 5.2. According to the results of previous studies, the bubbles in water were relatively large in Re and relatively small in $C_D$, which is consistent with the results obtained in this experiment. In water, the Re of the bubbles is mainly concentrated in the range 1000–3600, while the drag coefficients are all less than 3.5. As the Reynolds number increases, the drag coefficient drops to a minimum and then stabilizes. The data obtained in this experiment can show that the overall trend of the bubble tracing coefficient in water, and in 70%, glycerol solution is similar to Turton's equation, but differs somewhat from the Turton curve in terms of absolute values, which is related to the different media properties of the liquid. Therefore, this paper proposes a modified equation (16) based on experimental data with the liquid being water and 70% glycerol solution, and the modified equation is closer to the experimental results.

The experimental data indicate that in a 70% glycerol solution, the bubble Re is below 350, and the $C_D$ ranges between 2.3 and 5.2. Consistent with the findings of previous studies, bubbles in water exhibit a relatively high Re and a relatively low $C_D$. In water, the Re of the bubbles is predominantly concentrated within the range of 1000–3600, while the drag coefficients are all below 3.5. As the Reynolds number increases, the drag coefficient declines to a minimum before stabilizing.

The data obtained in this experiment demonstrate that the overall trend of the bubble drag coefficient in water and in a 70% glycerol solution is similar to Turton's equation, but deviates from the Turton curve in terms of absolute values, which can be attributed to the distinct properties of the liquid media. Consequently, this study proposes a modified equation (16) based on experimental data involving water and a 70% glycerol solution. The modified equation more closely aligns with the experimental results.

$$C_D = \frac{24}{\mathrm{Re}}\left[1 + 0.659(\mathrm{Re} - 3)^{0.648}\right] + \frac{0.852}{1 + 16\,300(\mathrm{Re} - 3)^{-1.3}}. \tag{16}$$

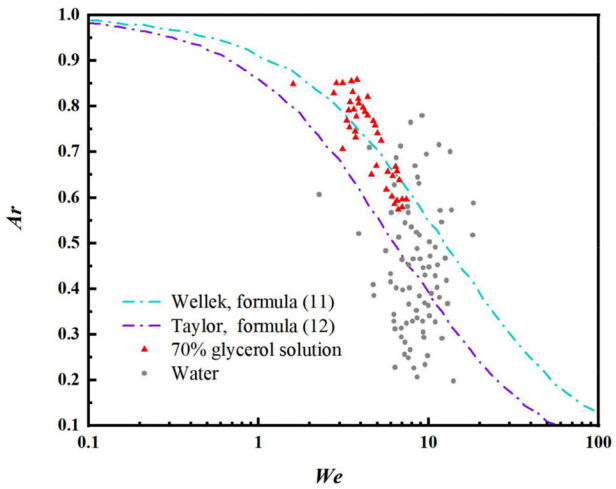


**FIG. 18.** Variation of bubble deformation *Ar* ratio with *We* during the experiment.

## E. Variation of fluid flow pattern inside bubbles of different shapes

As the bubble rises, its shape changes, and the fluid flow pattern within the bubble also undergoes transformation. The internal circulation flow presented inside the bubble results from the viscous resistance of the external fluid and the non-slipping nature of the internal fluid at the interface.[46,47] As previously mentioned, the study of fluid flow patterns inside bubbles of different shapes remains insufficient. In-depth research on the fluid flow pattern within regular-shaped

bubbles, such as spherical, elliptical, and spherical-cap-shaped bubbles, is scarce. For irregularly shaped bubbles, relevant research is still in its infancy. This section analyzes and summarizes the internal flow patterns of bubbles with different morphologies in various solutions, using numerical calculation results of bubble internal flow patterns.

In the 100% glycerol solution–air system, the deformation ratio of the bubble remains relatively stable, and its internal fluid flow can be clearly observed in Figs. 15 and 19(a). The gas inside the bubble rises in the middle, reaches the top, and flows down along the sides before converging from the sides to the middle when it returns to the bottom of the bubble. Consequently, two main vortices form inside the bubble, and this flow state is referred to as the double main vortex flow pattern. In the 70% glycerol solution, a similar internal flow pattern is present in the 2 and 4 mm bubbles, but in the 6 and 8 mm bubbles, when the deformation ratio is less than 0.445 [Fig. 13(c)], a separated vortex appears at the bottom, with a flow direction opposite to that of the main vortex [Fig. 19(b)].

In 70% glycerol solution, the 2 mm bubbles showed little change in shape after 0.1 s, and the internal flow pattern remains a double main vortex flow pattern. For larger diameter bubbles, their shape changes more drastically, and the flow pattern inside the bubble is complex. For the 4 mm bubble, the flow pattern inside the bubble changes from double main vortex to a "double main vortex with separation vortex" flow pattern. When the deformation ratio is lower than 0.7, the separation vortex starts to appear, indicating a correlation between the internal flow pattern and the bubble shape. For the 6 and 8 mm bubbles, the bubble flow pattern starts with a double main vortex flow pattern, with the double main vortex positioned at the tip of the spherical cap. However, as the bubble deformation occurs, the position of the main vortex and the separated vortex change.

As illustrated in Fig. 14, using the 6 mm bubble as an example, when the bubble first begins to move, its shape is spherical, and it displays a double main vortex flow pattern. As the spherical shape transforms into a spherical-cap shape and further into an upper semi-ellipse, the main vortex center moves downward along with the bubble's ends, and a separation vortex appears in the middle of the bubble. Between 0.05 and 0.125 s, the bubble shape shifts upward at both ends, and the separation vortex disappears due to the transition of the bubble to the upper semi-ellipse. After 0.15 s, the position of the separation vortex gradually moves toward both ends with the increase in the concavity at the middle bottom of the bubble, and the positions of the main vortex and the separation vortex continue to change with the alteration of the bubble shape.

In the 30% glycerol solution and water–air system, the flow pattern in the 2 mm bubble is double main vortex. However, in the 4, 6, and 8 mm bubbles, the flow pattern becomes more complex after 0.175 s due to the irregular deformation of the bubble. This is because the deformation ratio is too small, causing the bubble to adopt a striped shape. It becomes challenging to distinguish between the main vortex and separated vortex within the bubble. In this study, the vortex flow pattern in these irregularly shaped bubbles is referred to as the "scattered vortex" flow pattern [Fig. 19(c)]. As the bubble shape

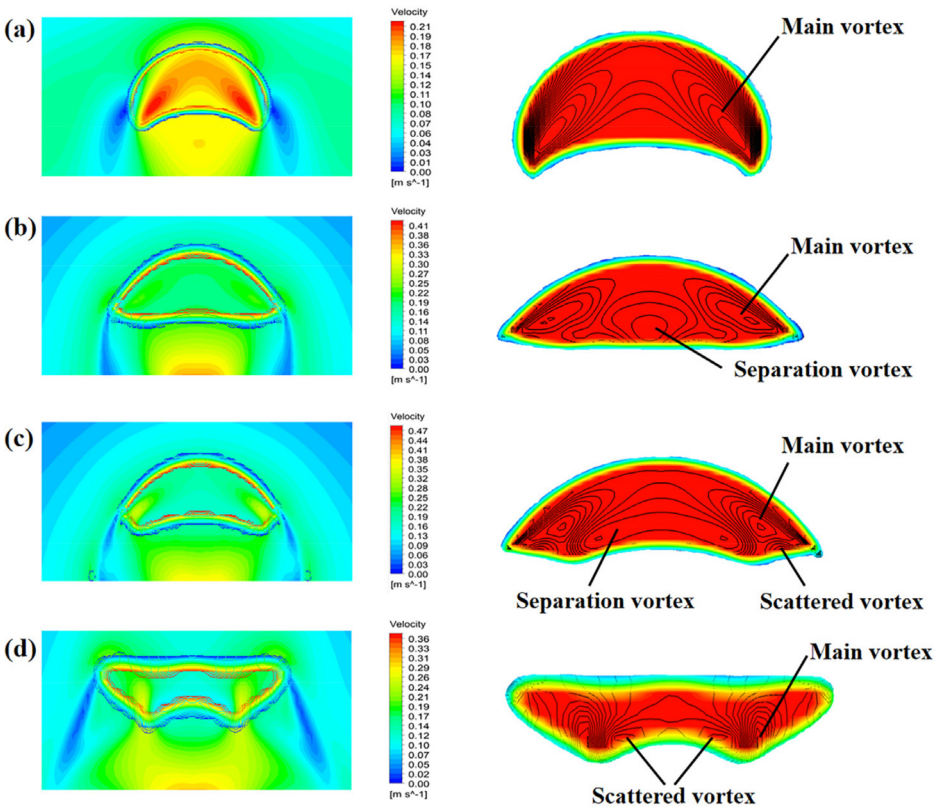


**FIG. 19.** Fluid flow pattern inside the bubble and velocity distribution inside the bubble: (a) 8 mm bubble in 100% glycerol solution at 0.2 s; (b) 6 mm bubble in 70% glycerol solution at 0.2 s; (c) 6 mm bubble in 30% glycerol solution at 0.25 s; and (d) 4 mm bubble in water at 0.35 s.

continues to evolve over time, it is observed that the scattered vortex is more likely to be present at bulging regions, although the size of the vortex may vary [Fig. 19(d)].

Figure 20 shows the maximum internal circulation velocity of different diameter bubbles in different gas–liquid systems. For the water–air system, the maximum internal circulation velocity of bubbles with different diameters varies significantly overall, particularly for 6 and 8 mm bubbles. This is because the bubble shape changes to a greater extent, and the space for airflow within the bubble is altered, thus affecting the internal circulation velocity. In the glycerol solution–air system with varying glycerol concentrations, the maximum internal circulation velocity of the bubbles decreases with increasing glycerol content. The increasing viscosity of the liquid results in less bubble deformation and reduced space for airflow within the bubble, thereby lowering the internal circulation velocity and the range of velocity fluctuations. Furthermore, by comparing the trends of the curves in Figs. 13 and 20, it can be concluded that the maximum internal circulation velocity is inversely related to the deformation ratio.

In the 70% glycerol solution, the inverse relationship between the maximum internal circulation velocity and the deformation ratio was found to be more pronounced. The relationship between the maximum internal circulation velocity and the deformation ratio for 4, 6, and 8 mm bubbles in 70% glycerol solution was summarized, and the following three sets of correlations were fitted based on the simulated value results: for 4, 6, and 8 mm bubbles, the correlations were Eqs. (17)–(19), respectively.

$$y = -1058.3x^6 + 4821.1x^5 - 10235x^4 + 11896x^3 - 6523.5x^2 + 3412.2x - 203.54, \quad (17)$$

$$y = -178.52x^6 + 756.4x^5 - 986.34x^4 + 826.7x^3 - 403.25x^2 + 126.79x - 64.35, \quad (18)$$

$$y = -105.34x^6 + 412.35x^5 - 841.59x^4 + 526.1x^3 - 186x^2 + 86.23x - 10.26, \quad (19)$$

where $x$ denotes the deformation ratio and $y$ denotes the maximum internal circulation speed.

The $R^2$ value is a variable that reflects the accuracy of the fitted correlations, with larger values indicating higher accuracy of the predicted correlations. Table IV shows the $R^2$ values for the different types of correlation equations, comparing the $R^2$ values for the four, five, and six equations. As the number of equations increases, the $R^2$ values become larger and the accuracy of the correlation equations further improves, with $R^2$ values of 0.9868, 0.9926, and 0.9963, respectively.

By summarizing the velocity distribution inside the four different shaped bubbles, the following observations can be made: (1) regardless of whether the bubble is regular or irregular in shape, the velocity at

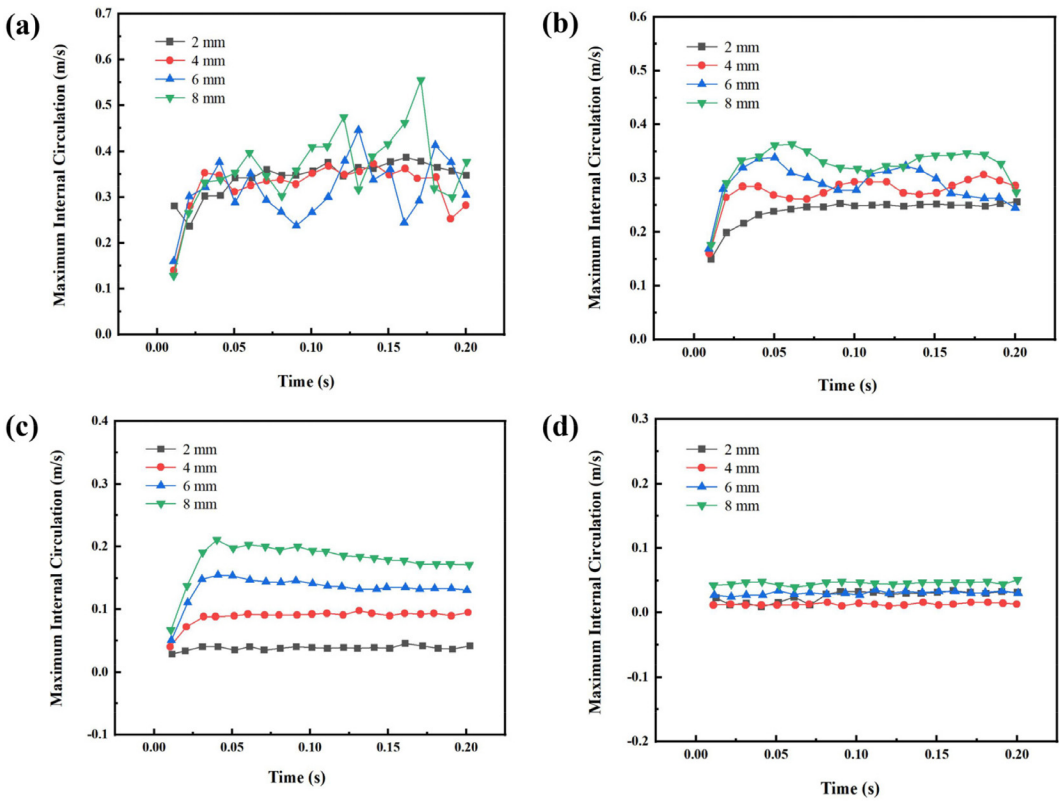


**FIG. 20.** Maximum internal circulation velocity of different diameter bubbles in different gas–liquid systems: (a) water; (b) 30% glycerol solution; (c) 70% glycerol solution; and (d) 100% glycerol.

**TABLE IV.** $R^2$ values for different types of associative equations.

| | $R^2$ value | Correlation formula |
|---|---|---|
| Quartic equation | 0.9868 | $y = -12.35x^4 + 35.68x^3 - 81.56x^2 + 25.18x - 4.35$ |
| Quintic equation | 0.9926 | $y = -39.58x^5 + 258.36x^4 - 164.3x^3 + 95.36x^2 - 56.27x + 7.56$ |
| Sextic equation | 0.9963 | $y = -105.34x^6 + 412.35x^5 - 841.59x^4 + 526.1x^3 - 186x^2 + 86.23x - 10.26$ |

both ends of the bubble is larger; (2) regardless of the type of vortex flow, the velocity at the vortex center is notably faster; (3) for the double main vortex with separated vortex flow pattern, the velocity at the center of the bubble is slower; and (4) when the interface of the bubbles adjacent to the dispersion vortex is bulging, the velocity at the interface is faster, if the adjacent interface is smooth, the velocity at the interface is slower.

From Figs. 19(a)–19(c), the maximum velocity inside each bubble gradually increases from 0.21 to 0.47 m/s, and the velocity distribution of the entire flow field correspondingly increases. These results confirm that the change in bubble shape leads to changes in the flow pattern within the bubble. As indicated by the flow patterns, an increase in fluid velocity inside the bubble promotes circulation within the flow field, which in turn increases the concentration gradient near the interface to facilitate mass transfer. The numerical simulation results are consistent with the bubble morphology change process captured in experiments, thus validating the accuracy of the simulation results.

## IV. CONCLUSIONS

This research focuses on analyzing the deformation trends of rising bubbles in stationary liquids and the fluid flow patterns within the bubbles. The volume-of-fluid method (VOF) numerical simulations and high-speed bubble visualization experiments are employed to assess the impact of bubble initial diameter, liquid viscosity, and surface tension on bubble deformation and internal fluid flow patterns. The morphological changes observed during the ascent of the bubbles in the numerical simulations are consistent with the high-speed visualization experiment results.

The findings reveal that as liquid viscosity increases, the bubbles rising speed decreases significantly, the length of the bubble motion trails increases, and the vortex position at both ends of the bubble gradually moves downward during the ascent. The bubble perturbation to the surrounding fluid is reduced, leading to a diminished deflection trend in the bubble motion trajectory. The bubble deformation ratio and the degree of fluctuation are influenced by the initial diameter of the bubbles, with an increase in bubble diameter leading to an increase in deformation ratio, and an increase in liquid phase viscosity resulting in a decrease in deformation ratio. Liquid viscosity primarily impacts bubble shape alteration, while liquid surface tension mainly affects bubble rupture. When the liquid surface tension is greater than $10^{-2}$ level N/m, bubbles deform without breaking. When the liquid surface tension is less than $10^{-2}$ level N/m, the bubble rupture and the number of ruptures increase as the surface tension decreases.

The flow patterns inside the bubble are classified into three main categories, double main vortex flow pattern, double main vortex with separated vortex flow pattern, and "double main vortex with scattered vortex" flow pattern. The analysis shows that the velocity is larger at the two ends of the bubbles and significantly faster at the center of the vortex for different vortex types. Generally, for the double main vortex with separated vortex flow type, the velocity at the center of the bubble is slower. The velocity at the interface is faster when the adjacent bubble interface is raised, and slower if the adjacent interface is smooth. By studying the deformation trend of the rising bubble and the flow pattern and velocity distribution inside the bubble, this work lays the foundation for the study of the flow field inside the bubble and improves the predictability of gas–liquid equipment design.

## AUTHOR DECLARATIONS

### Conflict of Interest

The authors have no conflicts to disclose.

### Author Contributions

Yixin Li and Na Yang contributed equally to this work.

**Yixin Li:** Writing – original draft (equal). **Na Yang:** Writing – original draft (equal). **Xiaoming Xiao:** Writing – review & editing (equal). **Bin Jiang:** Writing – review & editing (equal). **Yongli Sun:** Writing – review & editing (equal). **Luhong Zhang:** Writing – review & editing (equal).

## DATA AVAILABILITY

The data that support the findings of this study are available within the article.

## REFERENCES

[1]R. H. Chen, W. X. Tian, G. H. Su, S. Z. Qiu, Y. Ishiwatari, and Y. Oka, "Numerical investigation on coalescence of bubble pairs rising in a stagnant liquid," Chem. Eng. Sci. **66**, 5055 (2011).
[2]P. Chen, M. P. Dudukovi, and J. Sanyal, "Three-dimensional simulation of bubble column flows with bubble coalescence and breakup," AIChE J. **51**, 696 (2005).
[3]F. Chu, L. Yang, X. Du, and Y. Yang, "Mass transfer and energy consumption for $CO_2$ absorption by ammonia solution in bubble column," Appl. Energy **190**, 1068 (2017).
[4]B. Cui, B. Ni, and Q. Wu, "Bubble–bubble interaction effects on dynamics of multiple bubbles in a vortical flow field," Adv. Mech. Eng. **8**, 168781401663170 (2016).
[5]S. Wang, Q. Gui, J. Zhang, Y. Gao, J. Xu, and X. Jia, "Theoretical and experimental study of bubble dynamics in underwater explosions," Phys. Fluids **33**, 126113 (2021).
[6]W. Liang, R. Chen, J. Zheng, X. Li, and F. Lu, "Interaction of two approximately equal-size bubbles produced by sparks in a free field," Phys. Fluids **33**, 067107 (2021).
[7]L. Gemello, V. Cappello, F. Augier, D. Marchisio, and C. Plais, "CFD-based scale-up of hydrodynamics and mixing in bubble columns," Chem. Eng. Res. Des. **136**, 846 (2018).

[8]X. Guan and N. Yang, "Bubble properties measurement in bubble columns: From homogeneous to heterogeneous regime," Chem. Eng. Res. Des. **127**, 103 (2017).
[9]L. Zhang, Z. Zhou, J. Deng, and X. Shao, "A numerical study on the drag law of a gas bubble using dynamic body force method," Phys. Fluids **33**, 063320 (2021).
[10]N. Hasan and Z. B. Zakaria, "Computational approach for a pair of bubble coalescence process," Int. J. Heat Fluid Flow **32**, 755 (2011).
[11]Y. Hallez and D. Legendre, "Interaction between two spherical bubbles rising in a viscous liquid," J. Fluid Mech. **673**, 406 (2011).
[12]A. Desai, S. Mittal, and S. Mittal, "Experimental investigation of vortex shedding past circular cylinder in the high subcritical regime," Phys. Fluids **32**, 014105 (2020).
[13]A. R. Premlata, M. K. Tripathi, and K. C. Sahu, "Dynamics of rising bubble inside a viscosity-stratified medium," Phys. Fluids **27**, 072105 (2015).
[14]R. Kipping, M. Wagner, and U. Hampel, "On inter-bubble distances and bubble clustering in bubbly Flows: An experimental study," Chem. Eng. J. **431**, 133486 (2022).
[15]T.-J. Lin and G.-M. Lin, "Mechanisms of in-line coalescence of two-unequal bubbles in a non-Newtonian fluid," Chem. Eng. J. **155**, 750 (2009).
[16]M. K. Tripathi, K. C. Sahu, and R. Govindarajan, "Dynamics of an initially spherical bubble rising in quiescent liquid," Nat. Commun. **6**, 6268 (2015).
[17]D. M. Sharaf, A. R. Premlata, M. K. Tripathi, B. Karri, and K. C. Sahu, "Shapes and paths of an air bubble rising in quiescent liquids," Phys. Fluids **29**, 122104 (2017).
[18]Z. Liu, Y. Zheng, L. Jia, and Q. Zhang, "Study of bubble induced flow structure using PIV," Chem. Eng. Sci. **60**, 3537 (2005).
[19]S. Yamoah, C. K. Owusu-Manu, and E. H. K. Akaho, "Numerical investigation of bubble interaction mechanisms in gas–liquid bubbly flows: Harmonisation of bubble breakup and coalescence effects," Int. J. Multiphase Flow **144**, 103781 (2021).
[20]H. Mirsandi, G. Kong, K. A. Buist, M. W. Baltussen, E. A. J. F. Peters, and J. A. M. Kuipers, "Numerical study on the interaction of two bubbles rising side-by-side in viscous liquids," Chem. Eng. J. **410**, 128257 (2021).
[21]Y. Song, J. Zhu, C. Zhang, Z. Sun, and X. Lu, "Comparison of liquid–solid flow characteristics in upward and downward circulating fluidized beds by CFD approach," Chem. Eng. Sci. **196**, 501 (2019).
[22]H. Nazari-Mahroo, K. Pasandideh, H. A. Navid, and R. Sadighi-Bonabi, "How important is the liquid bulk viscosity effect on the dynamics of a single cavitation bubble?," Ultrason. Sonochem. **49**, 47 (2018).
[23]M. Wu and M. Gharib, "Experimental studies on the shape and path of small air bubbles rising in clean water," Phys. Fluids **14**, L49 (2002).
[24]T. Sirino, V. Machado, E. Mancilla, and R. E. M. Morales, "Dynamics of single bubbles rising in confined square and rectangular channels," Int. J. Multiphase Flow **157**, 104257 (2022).
[25]H. Zhang, K. Guo, Y. Wang, A. Sayyar, and T. Wang, "Numerical simulations of the effect of liquid viscosity on gas–liquid mass transfer of a bubble column with a CFD-PBM coupled model," Int. J. Heat Mass Transfer **161**, 120229 (2020).
[26]C. Zhang and I. Menshov, "Eulerian modelling of compressible three-fluid flows with surface tension," Russ. J. Numer. Anal. Math. Modell. **34**, 225 (2019).
[27]F. Risso, "Agitation, mixing, and transfers induced by bubbles," Annu. Rev. Fluid Mech. **50**, 25 (2018).
[28]N. Ochiai and J. Ishimoto, "Numerical analysis of the effect of bubble distribution on multiple-bubble behavior," Ultrason. Sonochem. **61**, 104818 (2020).
[29]A. R. Premlata, M. K. Tripathi, B. Karri, and K. C. Sahu, "Numerical and experimental investigations of an air bubble rising in a Carreau–Yasuda shear-thinning liquid," Phys. Fluids **29**, 033103 (2017).
[30]D. Funfschilling and H. Z. Li, "Effects of the injection period on the rise velocity and shape of a bubble in a non-Newtonian fluid," Chem. Eng. Res. Des. **84**, 875 (2006).
[31]L. Zhang, C. Yang, and Z.-S. Mao, "Numerical simulation of a bubble rising in shear-thinning fluids," J. Non-Newtonian Fluid Mech. **165**, 555 (2010).
[32]A. R. Premlata, M. K. Tripathi, B. Karri, and K. C. Sahu, "Dynamics of an air bubble rising in a non-Newtonian liquid in the axisymmetric regime," J. Non-Newtonian Fluid Mech. **239**, 53 (2017).
[33]Y. Li, J. P. Zhang, and L. S. Fan, "Discrete-phase simulation of single bubble rise behavior at elevated pressures in a bubble column," Chem. Eng. Sci. **55**, 4597 (2000).
[34]M. Rahman, K. Hasan, and H. Pan, "Capturing transition around low-Reynolds number hydrofoil with zero-equation transition model," Phys. Fluids **34**, 074115 (2022).
[35]N. Takagaki and S. Komori, "Air–water mass transfer mechanism due to the impingement of a single liquid drop on the air–water interface," Int. J. Multiphase Flow **60**, 30 (2014).
[36]X. Liu, L. Wang, and W. Ge, "Meso-scale statistical properties of gas-solid flow–A direct numerical simulation (DNS) study," AIChE J. **63**, 3 (2017).
[37]T. Saito and M. Toriu, "Effects of a bubble and the surrounding liquid motions on the instantaneous mass transfer across the gas–liquid interface," Chem. Eng. J. **265**, 164 (2015).
[38]M. Moragues Ginard, G. Bernardino, M. Vázquez, and G. Houzeaux, "Fourier stability analysis and local Courant number of the preconditioned variational multiscale stabilization (P-VMS) for Euler compressible flow," Comput. Methods Appl. Mech. Eng. **301**, 28 (2016).
[39]V. T. Nguyen, C.-H. Song, B.-U. Bae, and D.-J. Euh, "Modeling of bubble coalescence and break-up considering turbulent suppression phenomena in bubbly two-phase flow," Int. J. Multiphase Flow **54**, 31 (2013).
[40]Y. Zhao, X. Li, J. Cheng, C. Yang, and Z.-S. Mao, "Experimental study on liquid–liquid macromixing in a stirred tank," Ind. Eng. Chem. Res. **50**, 5952 (2011).
[41]C. Tang, P. Zhang, and C. K. Law, "Bouncing, coalescence, and separation in head-on collision of unequal-size droplets," Phys. Fluids **24**, 022101 (2012).
[42]K. L. Tse, T. Martin, C. M. Mcfarlane, and A. W. Nienow, "Small bubble formation via a coalescence dependent break-up mechanism," Chem. Eng. Sci. **58**, 275 (2003).
[43]M. W. Hlawitschka, P. Kováts, B. Dönmez, K. Zähringer, and H. J. Bart, "Bubble motion and reaction in different viscous liquids," Exp. Comput. Multiphase Flow **4**, 26 (2022).
[44]Z. Yu, H. Yang, and L.-S. Fan, "Numerical simulation of bubble interactions using an adaptive lattice Boltzmann method," Chem. Eng. Sci. **66**, 3441 (2011).
[45]G. Kelbaliyev and K. Ceylan, "Development of new empirical equations for estimation of drag coefficient, shape deformation, and rising velocity of gas bubbles or liquid drops," Chem. Eng. Commun. **194**, 1623 (2007).
[46]J. Liu, C. Zhu, T. Fu, Y. Ma, and H. Li, "Numerical simulation of the interactions between three equal-interval parallel bubbles rising in non-Newtonian fluids," Chem. Eng. Sci. **93**, 55 (2013).
[47]X. Wang, H. Dong, X. Zhang, L. Yu, S. Zhang, and Y. Xu, "Numerical simulation of single bubble motion in ionic liquids," Chem. Eng. Sci. **65**, 6036 (2010).